INTERNATIONAL JOURNAL FOR NUMERICAL METHODS IN ENGINEERING
*Int. J. Numer. Meth. Engng* (2012)
Published online in Wiley Online Library (wileyonlinelibrary.com). DOI: 10.1002/nme.4430

# A three-dimensional atomistic-based process zone model simulation of fragmentation in polycrystalline solids

Bo Ren[1,2] and Shaofan Li[1,3,*,†]

[1]*Department of Civil and Environmental Engineering, The University of California, Berkeley, CA 94720, USA*
[2]*School of Hydropower and Information Engineering, Huazhong University of Science and Technology, Wuhan 430074, China*
[3]*School of Civil Engineering and Engineering Mechanics, Huazhong University of Science and Technology, Wuhan 430074, China*

## SUMMARY

A three-dimensional atomistic-based process zone model (APZM) is used to simulate high-speed impact induced dynamic fracture process such as fragmentation and spall fracture. This multiscale simulation model combines the Cauchy–Born rule, colloidal crystal process model, and micromechanics homogenization technique to construct constitutive relations in both grains and grain boundary at mesoscale. The proposed APZM has some inherent advantages to describe mechanical behaviors of polycrystalline solids. First, in contrast to macroscale phenomenological constitutive models, the APZM takes into account atomistic binding energy and atomistic lattice structure. In particular, the electron density related embedded atom method (EAM) potential has been adopted to describe interatomistic interactions of metallic polycrystalline solids in bulk elements; second, a mixed type of EAM potential and colloidal crystal depletion potential is constructed to describe heterogeneous microstructure in the process zone; third, the atomistic potential in both bulk material and process zone has the same atomistic origin, and hence, the bulk and process potentials are self-consistent. The simulation of dynamic fracture process of a cylinder made of aluminum powder metallurgy (P/M) alloy during high-speed impact/penetration is carried out, and numerical results demonstrate that APZM finite element method has remarkable ability to accurately capture complex three-dimensional fragmentation formation and damage morphology. Copyright © 2012 John Wiley & Sons, Ltd.

Received 20 December 2011; Revised 28 May 2012; Accepted 17 September 2012

KEY WORDS: atomistic simulation; EAM potential; fragmentation; multiscale simulation; polycrystalline solid; process zone model

## 1. INTRODUCTION

In modern engineering, metallic polycrystalline materials are extensively used in aerospace, civil, electrical and computer, mechanical, and defense industries. The strength of polycrystalline materials is the key material property that is essential in design, manufacture, performance, and reliability of many devices, machineries, equipments, and vehicles. The simulation of defect evolution has been a critical part of computational materials science and computational failure mechanics of polycrystalline materials [1–3].

Consider crystallographic morphology of polycrystalline solids that each grain may have different atomistic structures, lattice orientations, shapes, and sizes, and the grain boundaries are inhomogeneous material zones with finite width, which may contain bimaterial interfaces, slip lines, defects, and inclusions. It is well known that microstructure characteristics such as grain shape,

---

*Correspondence to: Shaofan Li, Department of Civil and Environmental Engineering, The University of California, Berkeley, CA 94720, USA.

†E-mail: li@ce.berkeley.edu

Copyright © 2012 John Wiley & Sons, Ltd.

spatial arrangement, and local crystallographic orientation can influence materials properties at macroscale [4, 5].

To model materials' failure process, currently there are three distinctly different approaches corresponding material characteristics at different scales. At macroscale, there are many continuum material damage models available that are based on homogenization of microscale material properties or phenomenological theories [4–7]. However, the continuum model lacks rigorous description of roles of lattice orientations of grains and effects of crystal morphology on failure process [2, 8]. At microscale, the first principle based molecular dynamics (MD) can capture some fundamental features of materials behaviors, but because of its inherent high computational expense, even with today's computer and computational technology, it is still almost impossible to carry out an MD simulation of an atomistic system at cubic millimeter size scale [9]. From microscale to mesoscale, several multiscale methods have been developed, for example, [10], attempting to couple the quantum, atomistic, and continuum descriptions of matter for a unified treatment. Xiao and Belytschko [11] proposed a bridging domain method to couple continuum models with molecular models. Other notable state-of-the-art multiscale methods include the bridging scale method [12] and the multiscale field theory [13–15]. On the other hand, we have not seen many multiscale methods that are designed for macroscale polycrystalline solids. In literature, some researchers have studied mechanical responses of polycrystalline solid by examination of cohesive interaction between adjacent grains by using the phenomenological cohesive zone model (CZM), e.g., [2, 16, 17]. In these studies, usually phenomenological traction–separation cohesive laws between grains are used to control the fracture behavior.

Although there are several computational methods that have been developed to simulate progressive material surface separation during fracture, such as using extended finite element method (FEM) [18] and mesh free method [19, 20]. All these methods need additional and complicated computational algorithms to deal with evolving computation domain. However, during fragmentation process, the material may be disintegrated into many pieces; it is impossible to develop an analytical algorithm to manage such massive and complex material configuration evolving process. An alterative approach is the CZM [21], which is a finite element version of classical cohesive crack model developed by Dugdale [22] and Barrenblatt [23]. Cohesive FEM splits bulk mesh automatically on the basis of the traction–separation cohesive law between two adjacent elements. As mentioned previously, the phenomenological CZM has become popular in material failure simulation at macroscale as well as mesoscale polycrystalline problem.

The conventional cohesive zone is mainly a mathematical or mechanical interface formalism that provides a set of empirical cohesive laws that are not directly related to the actual physical origin of cohesion and decohesion mechanism of solids [24]. Nevertheless, the current trend of the CZM starts to construct multiscale cohesive law on the basis of the material physical decohesion such as atomistic and molecular interactions [25–27]. Many experiments reveal that the failure process of brittle material accompany with small scale plastic deformation, in contrast to the ductile fracture with large-scale yield that leads to dramatic local plastic deformation [28]. For the irreversible plastic deformation, Ortiz and Pandolfi [29] constructed a class of irreversible phenomenological cohesive laws to predict crack growth at macroscale. In material modeling, the energy storage and release of brittle polycrystalline solids may be approximated as deformation path independent; that is, the constitutive relation could be constructed from a stored potential energy function. With this assumption, Zeng and Li [30] and Li *et al.* [31] presented a multiscale process zone model that used the atomistic potential to build the bulk constitutive relation with the Cauchy–Born rule. Moreover, in process elements, they adopt a depletion potential approach to construct the self-consistent cohesive law inside the process zone. Subsequently, Qian and Li [3], He and Li [32] and Li *et al.* [31] applied this model to simulate two-dimensional (2D) and three-dimensional (3D) fracture and crack propagations in polycrystalline solids, and they discussed convergence problem and the mesh-size effect of this model as well. In this paper, the term process zone is used interchangeably with the term interphase zone.

In an early approach [30], only the electron density-independent pair-wise potentials are used in the process zone model, such as Lennard–Jones potential, which suffer from several shortcomings when simulating polycrystalline materials. For example, it is not true that the vacancy formation energy is always equal to the cohesive energy as predicted by the pair-wise potential approach [33]. As an extended version from pair potential, the embedded atom method (EAM) potential [34, 35] provides more accurate description of interatomic reactions by taking into account the effects of electron density distribution. Since 1990s, several EAM potentials have been developed to fit with the experimental data for a wide range of materials with different lattice structures, for example, face centered cubic (FCC) [36, 37], body centered cubic (BCC) [38], and hexagonal close packed (HCP) [37].

In this paper, we present a 3D atomistic-based process zone finite element formulation with the implementation of an EAM potential for simulation of fractures in polycrystalline solids. In the bulk element, we construct the mesoscale constitutive relation by using the Sutton–Chen (SC) potential (EAM), and in the process zone element, we build a mixed EAM-depletion potential to describe complex material degradation features inside grain boundaries or phase boundaries. On the basis of the foregoing atomistic potential, the so-called Cauchy–Born rule is used to establish the constitutive relation in both bulk and process zone elements, and then a mesoscale constitutive relation can be derived, from which stress tensors are obtained. Inspired by the concept of fracture process zone (FPZ), in this paper, we call our method as an atomistic-based process zone model (APZM) instead of an atomistic-based process zone model (AIZM) [31]. However, they may be used interchangeably.

This paper is organized in five sections: in Section 2, we describe the basic ideas and methods of the 3D multiscale process zone model; Section 3 focuses on constructing mesoscale constitutive equations on the basis of the EAM potentials in bulk and process zones that are related to the atomistic lattice structure; in Section 4, we discuss how to select the material constants, cohesive law, and equilibrium position for a polycrystalline aluminum solid. The results of numerical simulation of fragmentation are presented as well. Finally, a few remarks are made in Section 5.

## 2. THREE-DIMENSIONAL PROCESS ZONE FINITE ELEMENT MODEL

### 2.1. *The structure of atomistic-based process finite element method*

Following the same idea presented in [30], we are interested in developing a 3D multiscale process zone model. A polycrystalline solid consists of many grains and grain boundaries, and each grain

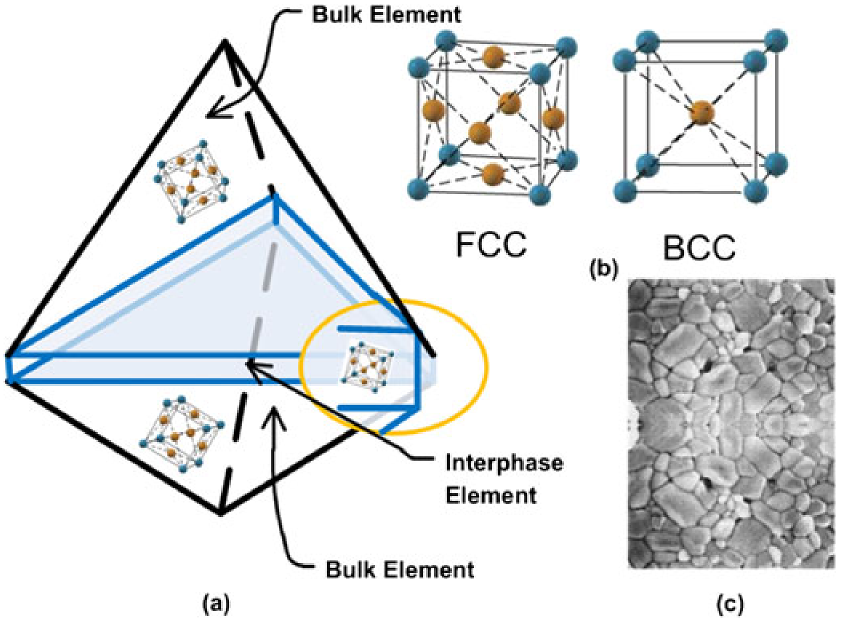

Figure 1. Schematic illustration of the concept of the process zone model: (a) the tetrahedral bulk element (black) and pentahedral process element (blue); (b) the lattice structure assigned to elements; (c) crystallographic morphology of brittle polycrystalline solid.

Copyright © 2012 John Wiley & Sons, Ltd.

has different shape, size, and crystallographic orientation as shown in Figure 1(c). In 2D cases, Voronoi tessellation is used to generate the geometric configuration of polycrystal grains [3], where the grain boundaries are defined as the finite width zones between Voronoi cells. Subsequently, each Voronoi cell can be divided into several triangle elements. However, to the authors' best knowledge, because of some technical difficulties, 3D Voronoi tessellation has not been used in generating 3D polycrystalline grain formation, and it is mainly used as a means for computer graphic visualization. In this work, to simplify the computational procedure, we use the tetrahedral element to represent 3D grains, and all four surfaces of a tetrahedral element are surrounded by four different wedge shape process elements, which are the representation of grain boundaries.

The mesh configuration of process zone model is schematically illustrated in Figure 1. The tetrahedral mesh can be easily generated as a normal FEM mesh. As depicted in Figure 1, the complex geometrical shapes of grains are simply represented by tetrahedral elements; that is, the whole computational domain is discretized by a tetrahedral mesh. Consequently, all surfaces of the tetrahedral elements are considered as grain boundaries; that is, for one grain inside the solid, there are four process elements (pentahedral element) surrounding it; the blue-color zone shown in Figure 1(a) is formed by the interface of two adjacent tetrahedral element; Figure 1(a) only shows one process zone element. This pentahedral (triangular prism) element is invisible in initial mesh, because it is a subscale element. A finite width is assigned to each process element in contrast with conventional CZM, in which the cohesive zone is considered as a virtual zone without width. Meanwhile, corresponding to different materials, different atomistic lattice structures are assigned to the bulk element as shown in Figure 1(b). Lattice structure is an ordered spatial arrangement of atom distribution; it can be represented by spatial replication of the unit cell. Figure 1(b) illustrates the unit cell of most popular lattice structure: FCC lattice and BCC lattice in 3D problem. To characterize the randomness of grain distribution, in addition to different volume to different grain, lattice orientation of each grain also randomly changes as shown in Figure 1(a).

Inside the grain boundary, the lattice structure or the spatial arrangement as well as distribution of atoms become even more complex. Here, a certain part of atoms remain the same lattice structure as in bulk elements, whereas the lattice structure of other part may vanish because of defects or incompatible arrangement. Therefore, atoms may become relatively sparse inside the grain boundary. However, considering the fact that most of atoms are in a certain lattice structure, hereby, a lattice structure or, more precisely, an effective supper-lattice structure is assigned to the process zone as shown in Figure 1(a).

In this work, we assume that the local nonuniform deformation is confined within grain boundaries. By deploying process zones around the bulk elements, the globally nonuniform deformation field is divided into locally uniform deformed bulk elements and locally nonuniform deformed process elements. Because the deformation inside bulk elements is uniform, the tetrahedral elements are adopted for the bulk elements. Otherwise, the deformations inside process elements are nonuniform; high order interpolation elements are used for process elements. In this work, we choose the six-node wedge element (C3D6) as the process element, which is compatible with the adjacent bulk tetrahedral elements. By doing so, we avoid to use the so-called discontinuous jump operator approach that is commonly employed in conventional CZM, in which interface element is a virtual entity that has no thickness because it is specifically designed to describe the cleavage fracture [21].

### 2.2. *Cauchy continuum and Cauchy–Born rule*

The proposed atomistic-based process zone model (APZM) constructs mesoscale material constitutive relation from microscale atomistic potentials in both grains and grain boundaries. The basic ideal is as follows: we can treat the grain as a type of Cauchy continuum because it deforms uniformly. By knowing the local deformation gradient and lattice structure at each grain, one can determine atomistic motion and hence material response motion uniquely in grain size, although the situation will become more complex in the grain boundary because of nonlinearity of deformation. Meanwhile, the so-called Cauchy–Born rule is employed to describe the kinematic behavior of polycrystalline solid as illustrated in Figure 2.

Although the Cauchy–Born rule may only apply when the local deformation is uniform, the proposed APZM applies it to each quadrature points in an element; Consequently, the global

Copyright © 2012 John Wiley & Sons, Ltd.

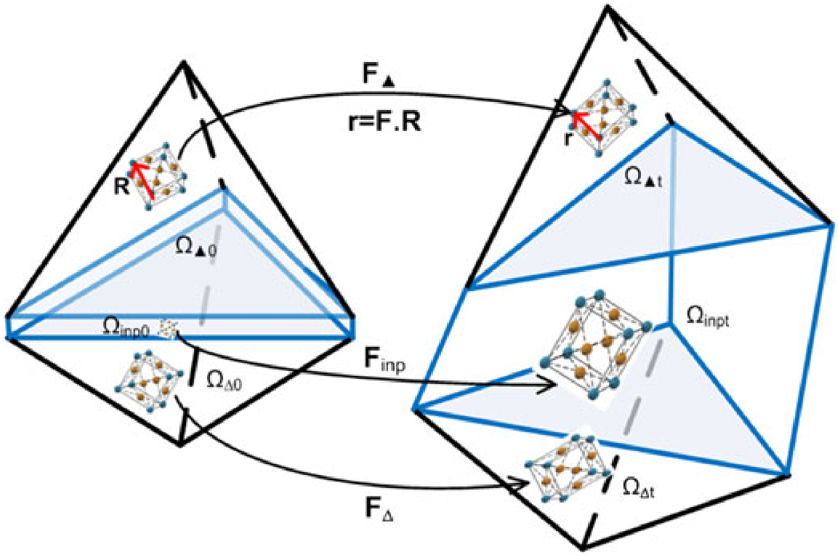

Figure 2. The Cauchy–Born rule.

nonuniform deformation field may be represented well by local piece-wise uniform deformation at the element level. For a given element (bulk element or process element) $e$, $e = 1, 2, 3, \ldots, nelem$, if the deformation inside each element is uniform, the deformation gradient, $\mathbf{F}_e$, is then a unique second-order tensor. We assume that the same type of atoms resides in an element, and they are assigned to a unique and specified lattice structure. As the lattice structure shown in Figure 1(b), for a given atom, it has $n_b$ neighbor atoms. Assume that the position vector of $i$th neighbor atom from the center atom is $\mathbf{R}_i$ (We also call it as the bond vector in this paper) in the reference (undeformed) configuration. The Cauchy–Born rule refers to the fact that the deformed position vector $\mathbf{r}_i$ in the current (deformed) configuration can be obtained by the following expression,

$$\mathbf{r}_i = \mathbf{F}_e \mathbf{R}_i \qquad i = 1, 2, 3, \ldots, n_b \tag{1}$$

where $\mathbf{F}_e = {}^{\partial \mathbf{x}}/_{\partial \mathbf{X}}$ is deformation gradient in the $e$th element.

With the Cauchy–Born rule, the deformed lattice bond may be determined by the deformation gradient $\mathbf{F}_e$ in an element. Therefore, for a crystalline solid, the elastic energy density in a given element can be represented by the potential energy density in a unit cell:

$$W_e(\mathbf{F}_e) = \frac{1}{\Omega_0} E(\mathbf{r}_i) = \frac{1}{\Omega_0} E(\mathbf{F}_e \cdot \mathbf{R}_i) \qquad i = 1, 2, 3, \ldots, n_b \tag{2}$$

Being consistent with continuum mechanics concept, we use the original volume of the unit cell, $\Omega_0$, to calculate the elastic energy density. $E(\mathbf{r}_i)$ is the atomistic potential function, and it can be the pair potential, for example, L-J potential, or other forms of atomistic potential, such as multibody EAM potentials [39, 40].

The fact of fracture without plastic deformation in a brittle material implies that its dynamic response is independent with deformation path. Consequently, the constitutive relation can be derived from energy density function:

$$\mathbf{S} = 2\frac{\partial W_e(F_e)}{\partial \mathbf{C}} = \frac{1}{\Omega_0}\frac{\partial E(r_i)}{\partial r_i}\frac{\partial r_i}{\partial \mathbf{C}} = \frac{1}{\Omega_0}\frac{\partial E(r_i)}{\partial r_i}\frac{\mathbf{R}_i \otimes \mathbf{R}_i}{r_i} \qquad i = 1, 2, 3, \ldots, n_b \tag{3}$$

where $\mathbf{S}$ is the second Piola–Kirchhoff stress (**PK-II** stress tensor), $r_i = |\mathbf{r}_i|$ is the deformed bond lengthes inside the unit cell, and $\mathbf{C} = \mathbf{F}^{\mathbf{T}}\mathbf{F}$ is the right Cauchy–Green tensor.

Although the second Piola–Kirchhoff stress with the symmetric property is convenient in constitutive modeling, it results a cumbersome expression in the equation of motion. Alternatively, the first Piola–Kirchhoff stress $\mathbf{P}$ is a suitable choice to be used in establishing the Galerkin weak form for balance of linear momentum:

$$\mathbf{P} = \mathbf{FS} = \frac{1}{\Omega_0}\frac{\partial E(r_i)}{\partial r_i}\frac{\mathbf{R}_i \otimes \mathbf{r}_i}{r_i} \qquad i = 1, 2, 3, \ldots, n_b \tag{4}$$

### *2.3. The deformation gradient in bulk and process zone*

The mesoscale or macroscale stress expressions for bulk elements and process zone are derived from atomistic potential. One may find that both the elastic energy density and the stress expression in Equations (3) and (4) are the function of deformation gradients $\mathbf{F}_e$, which are calculated differently for bulk and process elements.

The deformation gradient in the bulk element, $\mathbf{F}_b$, is calculated as

$$\mathbf{F}_b = \frac{\partial \mathbf{x}}{\partial \mathbf{X}} = \frac{\partial \mathbf{u}}{\partial \mathbf{X}} + \mathbf{I} \tag{5}$$

Here, $\mathbf{u}$ is the nodal displacements of bulk element.

The conventional CZM considers cohesive zone as a virtual zone without thickness [21]; the phenomenological cohesive law is usually given as an empirical formulation with open parameters fitted from experimental data [41]. To describe the coarse grain polycrystalline structure, the proposed APZM FEM assumes that the process zone region is a quasicrystalline layer with finite thickness $R_0$, which can be thought as a physical parameter related to the width of grain boundary or the width of persistent slip band. The value of $R_0$ depends on a given realistic crystallographic structure, and in this work, we consider that it varies in the range $10^{-5} \leqslant R_0/S_0 \leqslant 10^{-2}$; here, $S_0$ is the characteristic length of grains or bulk elements.

The deformation gradient in the process element $\mathbf{F}_{\mathrm{inp}}$ should be a nonlinear function of the position of material point $\mathbf{X}$ shown in Figure 3. However, the inhomogeneous deformation field inside the process element may be decomposed into two scales:

$$\mathbf{u_p} = \bar{\mathbf{u}} + \mathbf{u}' \tag{6}$$

where $\bar{\mathbf{u}}$ is the global homogeneous displacement field in coarse grain filed whereas $\mathbf{u}'$ is the inhomogeneous displacement fluctuation field. Then, the general deformation field in process zone can be described as

$$\mathbf{x} = \bar{\mathbf{F}}\mathbf{X} + \mathbf{u}' \tag{7}$$

where $\bar{\mathbf{F}}$ may be viewed as the coarse grain deformation gradient in the process zone. If one uses the idea of the Hill–Mandel lemma [42], it can be proved that the average deformation gradient $\langle \mathbf{F} \rangle_{\Omega_0}$ in a process zone element is exactly same as $\bar{\mathbf{F}}$:

$$\mathbf{F_p} = \langle \mathbf{F} \rangle_{\Omega_0} = \bar{\mathbf{F}} \tag{8}$$

In this work, we neglect the inhomogeneous displacement fluctuation field inside the process zone, let $\mathbf{F_p} = \bar{\mathbf{F}}$.

Because the process element shares nodes with adjacent bulk elements, the coarse scale deformation field $\mathbf{F}_{\mathrm{inp}}$ could be compatible with the motion of bulk elements by an affine function. Assume there is a vector $\mathbf{x}$ at current process element; it can be determined by affine mapping from original position $\mathbf{X}$:

$$\mathbf{x} = \mathbf{F_p}\mathbf{X} + \mathbf{a} \tag{9}$$

To fix rigid body motion, we set the $\mathbf{a} = 0$. In Equation (9), $\mathbf{F}_{\mathrm{inp}}$ has nine unknown variables in 3D problem; to solve them, we need to know deformation of three vectors. In Figure 3, we define coordinates of a six-node pentahedral element as $\mathbf{r_i} = (x_i, y_i, z_i)$ and $\mathbf{R_i} = (X_i, Y_i, Z_i)$ at deformed and undeformed field, respectively; these nodes actually are shared with the adjacent bulk elements too (see Figure 1(a)). Because all element nodal displacements can be calculated from

Copyright © 2012 John Wiley & Sons, Ltd.

DOI: 10.1002/nme

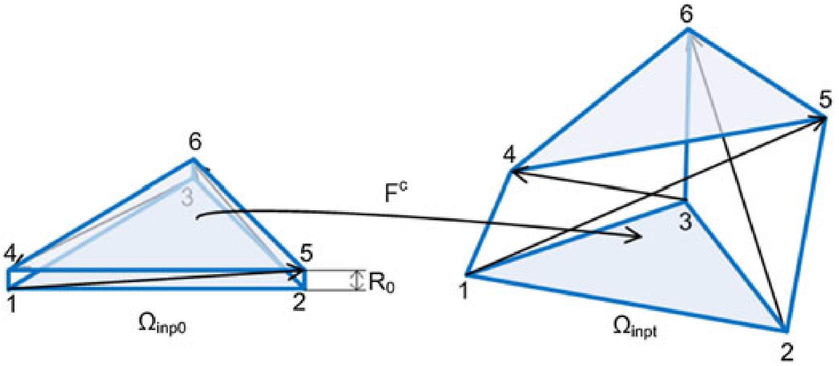

Figure 3. The effective deformation gradient in the process zone.

the bulk elements, we can calculate relative position vectors in process element. Denote the vectors $\mathbf{r}_{15}, \mathbf{r}_{26}, \mathbf{r}_{34}$ as the relative position vectors in a deformed process zone element as well as $\mathbf{R}_{15}, \mathbf{R}_{26}, \mathbf{R}_{34}$, which are known variables, shown in Figure 3. From Equation (9), we can establish the following geometric relationships:

$$\begin{aligned} \mathbf{r}_{15} &= \mathbf{F_p}\mathbf{R}_{15} \\ \mathbf{r}_{26} &= \mathbf{F_p}\mathbf{R}_{26} \\ \mathbf{r}_{34} &= \mathbf{F_p}\mathbf{R}_{34} \end{aligned} \tag{10}$$

Therefore, the components of $\mathbf{F_p}$ can be solved as

$$\begin{pmatrix} F_{11} \\ F_{12} \\ F_{13} \\ F_{21} \\ F_{22} \\ F_{23} \\ F_{31} \\ F_{32} \\ F_{33} \end{pmatrix} = \begin{bmatrix} \mathbf{A}^{-1} & 0 & 0 \\ 0 & \mathbf{A}^{-1} & 0 \\ 0 & 0 & \mathbf{A}^{-1} \end{bmatrix} \begin{pmatrix} x_1 - x_5 \\ x_3 - x_4 \\ x_2 - x_6 \\ y_1 - y_5 \\ y_3 - y_4 \\ y_2 - y_6 \\ z_1 - z_5 \\ z_3 - z_4 \\ z_2 - z_6 \end{pmatrix} \tag{11}$$

Here, $\mathbf{A}$ is a constant second-order tensor related to the nodal coordinates in reference configuration:

$$\mathbf{A} = \begin{bmatrix} X_1 - X_5 & Y_1 - Y_5 & Z_1 - Z_5 \\ X_3 - X_4 & Y_3 - Y_4 & Z_3 - Z_4 \\ X_2 - X_6 & Y_2 - Y_6 & Z_2 - Z_6 \end{bmatrix} \tag{12}$$

From Figure 3, one may find that the geometrical position of bulk elements and the thickness of process zone ($R_0$) determine the configuration of process element at reference configuration; that is, the length scale $S_0$ and $R_0$ are involved in the calculation of matrix $\mathbf{A}$ implicitly, and they also determine the deformation gradient of the process element.

### 2.4. *Finite element method implementation*

Considering a complete bulk-process domain, the Galerkin weak formulation of multiscale process zone model may be expressed as

$$\begin{aligned} &\sum_{e=1}^{n^b} \left\{ \int_{\Omega_0^e} \left( \rho_0 \ddot{\mathbf{u}}^h \cdot \delta\mathbf{u}^h + \mathbf{P}(\mathbf{u}) : \delta\mathbf{F}^h \right) \mathrm{d}V \right\} + \sum_{i=1}^{n^i} \left\{ \int_{\Omega_0^i} \left( \rho_0 \ddot{\mathbf{u}}^h \cdot \delta\mathbf{u}^h + \bar{\mathbf{P}} : \delta\bar{\mathbf{F}}^h \right) \mathrm{d}V \right\} \\ &\quad = \sum_{e=1}^{n^b} \left\{ \int_{\Omega_0^e} \mathbf{b} \cdot \delta\mathbf{u}^h \mathrm{d}V + \int_{\partial_t \Omega_o^e} \bar{\mathbf{T}} \cdot \delta\mathbf{u}^h \mathrm{d}\Gamma \right\} + \sum_{i=1}^{n^i} \left\{ \int_{\Omega_0^i} \mathbf{b} \cdot \delta\mathbf{u}^h \mathrm{d}V + \int_{\partial_t \Omega_o^i} \bar{\mathbf{T}} \cdot \delta\mathbf{u}^h \mathrm{d}\Gamma \right\} \end{aligned} \tag{13}$$

Copyright © 2012 John Wiley & Sons, Ltd.

where $n^b, n^i$ denote the number of bulk and process elements, respectively; $\mathbf{P}$ and $\bar{\mathbf{P}}$ are the first Piola–Kirchhoff stress in bulk and process element, respectively; $\mathbf{b}$ is the body force; and $\bar{\mathbf{T}}$ is the traction force. In the proposed APZM, the process zone element shares nodes with bulk elements, all material mass and body forces are lumped at those nodes. Therefore, we assume that the process zone is an interior zone; the traction force and body force only are applied to bulk elements. Then, Galerkin weak form can be simplified as

$$\begin{aligned}\sum_{e=1}^{n^b}\left\{\int_{\Omega_0^e}\left(\rho_0\ddot{\mathbf{u}}^h\cdot\delta\mathbf{u}^h+\mathbf{P}(\mathbf{u}):\delta\mathbf{F}^h\right)\mathrm{d}V\right\}+\sum_{i=1}^{n^i}\left\{\int_{\Omega_0^i}\bar{\mathbf{P}}:\delta\bar{\mathbf{F}}^h\mathrm{d}V\right\}\\=\sum_{e=1}^{n^b}\left\{\int_{\Omega_0^e}\mathbf{b}\cdot\delta\mathbf{u}^h\mathrm{d}V+\int_{\partial_t\Omega_o^e}\bar{\mathbf{T}}\cdot\delta\mathbf{u}^h\mathrm{d}\Gamma\right\}\end{aligned}\tag{14}$$

The second term of the left-hand side of the equation is the cohesive force that 'glues' bulk elements together. Applying the divergence theorem to process element, and because $R_0$ is a finite thickness, we can obtain cohesive traction force imposed at the bulk element in a surface integral:

$$\int_{\Omega_0^i}\bar{\mathbf{P}}:\delta\bar{\mathbf{F}}^h\mathrm{d}V=\int_{\partial B_0^e\cap\partial B_0^i}\mathbf{T}^{\mathrm{coh}}\cdot\delta\mathbf{u}\mathrm{d}\Gamma\tag{15}$$

Comparing with the separation–traction force cohesive law used in CZM, the cohesive traction, $\mathbf{T}^{\mathrm{coh}}$, in APZM is the traction on the surfaces of process elements that are adjacent to the bulk element, and it is calculated by the following expression:

$$\mathbf{T}^{\mathrm{coh}}=\bar{\mathbf{P}}\cdot\mathbf{N}\tag{16}$$

There are several advantages in this approach: (1) APZM is an intrinsic mixed-mode model in terms of fracture simulation. (2) The process constitutive behaviors are consistent with that of the bulk material. (3) By combining the Cauchy–Born rule with the process zone approach, we regularize the Cauchy–Born rule based continuum finite element approach, which has multiple minima at a local region.

Considering that the normal of process element surface $\mathbf{N}$ is opposite to that of the adjacent bulk element at reference configuration, we can write the Galerkin weak form as

$$\begin{aligned}\sum_{e=1}^{n^b}\left\{\int_{\Omega_0^e}\left(\rho_0\ddot{\mathbf{u}}^h\cdot\delta\mathbf{u}^h+\mathbf{P}(\mathbf{u}):\delta\mathbf{F}^h\right)\mathrm{d}V-\int_{\partial\Omega_0^e\cap\partial\Omega_0^c}\mathbf{T}^{\mathrm{coh}}\cdot\delta\mathbf{u}\mathrm{d}\Gamma\right\}\\=\sum_{e=1}^{n^b}\left\{\int_{\Omega_0^e}\mathbf{b}\cdot\delta\mathbf{u}^h\mathrm{d}V+\int_{\partial_t\Omega_o^e}\bar{\mathbf{T}}\cdot\delta\mathbf{u}^h\mathrm{d}\Gamma\right\}\end{aligned}\tag{17}$$

Consider following classic FEM interpolation in each bulk element

$$\mathbf{u}^h(\mathbf{X})=\sum_{I=1}^{n}\mathbf{N}_I(\mathbf{X})\mathbf{u}_I\tag{18}$$

Following the standard FEM discretization procedure, the discrete dynamic equation of motion is

$$\mathbf{M}\ddot{\mathbf{u}}+\mathbf{f}^{\mathrm{int}}(\mathbf{u})-\mathbf{f}^{coh}(\mathbf{u})=\mathbf{f}^{ext}\tag{19}$$

Copyright © 2012 John Wiley & Sons, Ltd.

DOI: 10.1002/nme

$$
\begin{aligned}
\mathbf{M} &= \mathop{\mathbf{A}}_{e=1}^{n_b} \int_{\Omega_0^e} \rho_0 \mathbf{N}^{eT} \mathbf{N}^e \mathrm{d}V \\
\mathbf{f}^{\mathrm{int}} &= \mathop{\mathbf{A}}_{e=1}^{n_b} \int_{\Omega_0^e} \mathbf{B}^e \mathbf{P}^e \mathrm{d}V \\
\mathbf{f}^{coh} &= \mathop{\mathbf{A}}_{e=1}^{n_b} \int_{\Omega_0^e \cap \partial \Omega_0^c} \mathbf{N}^{eT} \mathbf{T}^{\mathrm{coh}} \mathrm{d}S \\
\mathbf{f}^{ext} &= \mathop{\mathbf{A}}_{e=1}^{n_b} \int_{\Omega_0^e \cap \partial \Omega_0^c} \left\{ \int_{\Omega_0^e} \mathbf{N}^{eT} \mathbf{b} \mathrm{d}V + \int_{\partial_T \Omega_0^e} \mathbf{N}^{eT} \bar{\mathbf{T}}^E \mathrm{d}S \right\}
\end{aligned}
\tag{20}
$$

where $\mathbf{A}$ is the element assemble operator, $\mathbf{N}^e$ is the element shape function matrix, and $\mathbf{B}^e$ is the element B-matrix. Explicit time integration algorithm, Newmark-$\beta$ ($\beta = 0.5, \gamma = 0.0$), is used in time integration for the discrete dynamics equation (19) [43].

## 3. EMBEDDED ATOM METHOD POTENTIALS IN MULTISCALE PROCESS ZONE MODEL

### *3.1. Embedded atom method potential in bulk element*

With proper interatomistic potential, MD simulation can essentially calculate motions of atoms at microscale. However, because of the restriction of computational resource, a typical MD simulation domain may only has a size of few hundreds of cubic nanometers, which is far below the micron or millimeter scale (mesoscale), which is spatial scale region that this work is concerned with. Instead of calculating the interatomistic reaction atom by atom, the proposed APZM model assumes that each element has a definite atomistic lattice structure, and a piece-wise uniform deformation in bulk elements, so the Cauchy–Born rule can be adopted to construct constitutive relation from atomistic energy potential, as suggested in Equations (3) and (4).

One can find the total energy of a given atom by summing up all potential energy over its neighbor atoms [44]:

$$
E_T = \frac{1}{2} \sum_{i,j(i \neq j)} \varphi(\mathbf{r}_{ij}) \tag{21}
$$

However, in pair potentials, atomistic bonds are treated independent from each other, which is an approximation with the advantage of simple form of expressions. In real applications, such simple pair interaction may not be able to accurately describe the interatomistic relation for solids, especially metallic materials. This is because the electrons of metallic material are not localized around the nuclei, and in fact, the valence electrons, namely free-electron gas or electron glue, is shared among atoms. To capture this multibody feature of metallic materials, Daw and Baskes [34, 35] proposed a well-known remedy—the embedded atom method (EAM), which consists of the pair energy potential and the energy potential obtained by embedding an atom into a local electron density cloud provided by the existing atomic system. EAM potential provides a realistic description of the potential energy of an N-atoms metallic system, which may be written as follows [39],

$$
E_T = \sum_{i=1} F_i(\rho_i) + \frac{1}{2} \sum_{i} \sum_{i \neq j} \varphi(r_{ij}) \tag{22}
$$

Here, $\varphi(r_{ij})$ is a repulsive pair potential that corresponds to an effective ionic charge that depends on the interatomic distance $r_{ij}$ between atom *i*th and *j*th. $F_i(\rho_i)$ is the embedding function, which corresponds to the required energy to embed an atom into the existing N-atoms system at site *i*, where the electron density is $\rho_i$. Although EAM is actually a tabular potential, there are some analytical EAM models, such as SC model [39] and Oh–Johnson (OJ) model [37]. Comparing with the OJ-EAM potential, which provides accurate fault energy but poor elastic constants, the SC potential fits

Copyright © 2012 John Wiley & Sons, Ltd.

DOI: 10.1002/nme

to the lattice parameter, cohesive energy, and elastic constants very well [45]; therefore, we adopt SC potential [39] for aluminum materials:

$$E_T^b(r) = \varepsilon \left\{ \frac{1}{2} \sum_i \sum_{j \neq i} \left( \frac{\alpha}{r_{ij}} \right)^n - c \sum_i \sqrt{\rho_i} \right\} \tag{23}$$

where $\rho_i$ is electron density at the site of atom $i$th:

$$\rho_i(r) = \sum_{i \neq j} \left( \frac{\alpha}{r_{ij}} \right)^m \tag{24}$$

In a perfect lattice structure, the energy of a specified atom $i$th should be counted by

$$E_i^b(r) = \varepsilon \left\{ \frac{1}{2} \sum_{j \neq i} \left( \frac{\alpha}{r_{ij}} \right)^n - c \sqrt{\rho_i} \right\} \tag{25}$$

where $\varepsilon, c, \alpha, m, n$ are numerical values obtained from fitting Equation (25) to the ab initio calculation results for the most stable bulk configuration. Here, $j$ is the loop index of neighboring atoms of atom $i$th.

### *3.2. Embedded atom method based potential in the process zone*

In contrast with the homogenous deformation inside bulk grains, defects, inclusions, and other inhomogeneities makes the grain boundary a highly nonuniform deformed region, in which regular lattice structure and localized in-homogenous lattice structure coexist. Because of this, metallic bonds and the von der Waals bond may also coexist. By assuming that the process zone is a relatively 'porous' material zone between grains, we may assume that the atomistic potential inside the process zone is the linear combination of the bulk atomistic potential and the long-range atomistic interaction potential stemming from the atomistic pair potential—a colloidal crystal analog:

$$E_T^c = (1-\beta)E^b(r) + \beta E^c(r) \tag{26}$$

Here, $E^c$ represents the contribution of process potential due to the long-range atomistic interaction in the process zone, which reflects the impurity and porosity effects of the process, whereas $E^b(r)$ is the atomistic potential for the bulk material, which is exactly the same as bulk atomistic potential, for example, the SC-EAM potential in Equation (25). The variable $0 \leqslant \beta \leqslant 1$ is the proportionality constant of the long-range atomistic interaction potential in the total process potential. In fact, the essence of the depletion potential approach employed in this work is to interpret the cohesive force inside the grain or phase boundaries as a type of colloidal adhesive force. With this idea, we construct a long-range 'depletion potential' on the basis of long-range atomistic bond interaction to represent the potential energy in an inhomogeneous process zone:

$$E^c(r) = E^{\text{dep}}(r) \tag{27}$$

Here, the key is how to construct the depletion potential $E^{\text{dep}}(r)$. From Figure 3, one can find that there is a finite width $R_0$ of process zone region in this multiscale process zone model. The intermolecular interaction inside the process zone is a type of the van der Waals interaction between noncovalent bonds or quasicovalent bonds. The cohesive strength of the process zone can then be determined by the intermolecular forces in surrounding bulk medium. Under these assumptions, when calculating the interaction between two material points inside the process zone and the bulk medium, we may consider the bulk medium as rigid with almost no deformation. So the two bulk elements adjacent to the compliant process zone may be viewed as two rigid body half spaces. Here, the atomistic potential for a bulk medium is given as SC potential; we can obtain the depletion potential of the process zone by integrating the bulk potential over the rigid bulk medium half space [46] as shown in Figure 4:

Copyright © 2012 John Wiley & Sons, Ltd.

DOI: 10.1002/nme

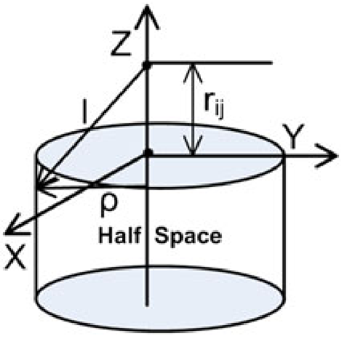

Figure 4. Integration scheme for acquiring the depletion potential in the process zone.

$$E^{\text{dep}}(r) = \int_{\text{Half Space}} \frac{1}{\Omega_0^b} W^b(r)\mathrm{d}V \tag{28}$$

Here, $W^b(r)$ is the pair potential part of the SC potential energy density for bulk elements, and $\Omega_0^b$ is the volume of the unit cell. The electron density part of the SC potential represents the field of electron gas or glue among atoms, which is the feature of metallic bulk materials, and it is partially present in the process zone according to $\beta$ as well. However, the metallic bond may not be approximated as long-range colloidal force. Therefore, only the pair part is considered in depletion integration.

Assuming that atom pairs are independent from each other, the depletion potential for the $i$th atom in process zone could be derived as

$$E_i^{\text{dep}}(r) = \int_{\Omega_{\text{HS}}} \frac{\varepsilon}{2\Omega_0^b} \sum_{j\neq i} \left(\frac{\alpha}{l}\right)^n \mathrm{d}V = \frac{\varepsilon}{2} \sum_{j\neq i} \int_{\Omega_{\text{HS}}} \frac{1}{\Omega_0^b} \left(\frac{\alpha}{l}\right)^n \mathrm{d}V \tag{29}$$

Here, $\Omega_0^b$ is the volume assigned to a bulk atom. Considering a cylindrical coordinate system, we have $\mathrm{d}V = \pi d\rho^2 \mathrm{d}z$ and $l = \sqrt{\rho^2 + (z - r_{ij})^2}$. Integrating Equation (29) over the half space, we can obtain the depletion potential as follows:

$$E_i^{\text{dep}}(r) = \frac{\varepsilon\pi\alpha^3}{\Omega_0^b(n-2)(n-3)} \sum_{i\neq j} \left(\frac{\alpha}{r_{ij}}\right)^{n-3} \tag{30}$$

Finally, an atomistic process potential that can characterize both porosity and impurity of the process and the effect of electron density is constructed. In specific, from Equations (25), (26), and (30), we can find the process zone atomistic potential for the $i$th atom in an equivalent unit cell as

$$E_i^c(r_{ij}) = (1-\beta)\varepsilon \left\{ \frac{1}{2} \sum_{j\neq i} \left(\frac{\alpha}{r_{ij}}\right)^n - c\sqrt{\rho_i} \right\} + \beta \frac{\varepsilon\pi\alpha^3}{\Omega_0^b(n-2)(n-3)} \sum_{i\neq j} \left(\frac{\alpha}{r_{ij}}\right)^{n-3} \tag{31}$$

From this derivation, one can see that the process zone potential is related or consistent with the bulk atomistic potential.

### *3.3. The constitutive relation in bulk and process zone*

Equations (25) and (31) provide the atomistic potentials for bulk elements and process zone elements. Subsequently, the Cauchy–Born rule is implemented to establish the constitutive relation for bulk element as well as process zone elements. Equation (3) provides the general expression that links atomistic potential to the second Piola–Kirchhoff (PK-II) stress tensor.

Copyright © 2012 John Wiley & Sons, Ltd.

DOI: 10.1002/nme

Substituting Equation (25) into Equation (3), we can obtain the second Piola–Kirchhoff stress in bulk elements as

$$\mathbf{S}^b = \frac{\varepsilon}{2\Omega_0^b\alpha^2}\left\{mc\left(\sum_i\left(\frac{\alpha}{r_i}\right)^m\right)^{-0.5}\sum_i\left(\frac{\alpha}{r_i}\right)^{m+2} - n\sum_i\left(\frac{\alpha}{r_i}\right)^{n+2}\right\}\mathbf{R_i}\otimes\mathbf{R_i}$$
$$i = 1, 2, 3, \ldots, n_b \tag{32}$$

where $n_b$ denotes the total neighboring atoms around one bulk atom.

Equation (31) describes the potential for process zone, and it is consistent with bulk potential in a sense that it is derived from it. Following the same process as bulk constitutive relation, the description of PK-II stress for process zone element is

$$\mathbf{S}^c = \frac{\varepsilon}{\Omega_0^c\alpha^2}\left\{(1-\beta)\left[\frac{mc}{2}\left(\sum_i\left(\frac{\alpha}{r_i}\right)^m\right)^{-0.5}\sum_i\left(\frac{\alpha}{r_i}\right)^{m+2} - \frac{n}{2}\sum_i\left(\frac{\alpha}{r_i}\right)^{n+2}\right]\right.$$
$$\left. - \beta\frac{\pi\alpha^3}{\Omega_0^b(n-2)}\sum\left(\frac{\alpha}{r_i}\right)^{n-1}\right\}\mathbf{R_i}\otimes\mathbf{R_i} \quad i = 1, 2, 3, \ldots, n_b \tag{33}$$

We then can obtain the first Piola–Kirchhoff (PK-I) stress:

$$\mathbf{P} = \mathbf{F}\cdot\mathbf{S} \tag{34}$$

where **F** is the deformation gradient in bulk or process zone element, respectively.

Equation (15) describes the traction stress $\mathbf{T}^{\text{coh}}$ at the surface of process zone ($\Delta 123$ and $\Delta 456$ in Figure 3). To calculate the cohesive force, consider PK-I stress at the reference configuration; one can find that $\Delta 123$ and $\Delta 456$ have opposite surface normal $\left(\mathbf{N}^{c\Delta 123} = -\mathbf{N}^{c\Delta 456}\right)$; then, $\mathbf{T}^{\text{coh}}$ should be

$$\mathbf{T}^{\text{coh}\Delta 123} = \mathbf{P}\cdot\mathbf{N}^{c\Delta 123} \quad \text{and} \quad \mathbf{T}^{\text{coh}\Delta 456} = -\mathbf{P}\cdot\mathbf{N}^{c\Delta 123} \tag{35}$$

Note that the mesoscale surface separation between $\Delta 123$ and $\Delta 456$ can be uniquely determined by the nodal displacements between nodes $1, 2, 3$ and nodes $4, 5, 6$. Let it be denoted as $\boldsymbol{\Delta}$. As shown in Equation (11), the average deformation gradient inside the process element is a function of $\boldsymbol{\Delta}$, that is, $\bar{\mathbf{F}}_{\text{inp}} = \bar{\mathbf{F}}(\boldsymbol{\Delta})$. Hence,

$$\mathbf{T}^{\text{coh}\Delta 123} = \mathbf{P}\cdot\mathbf{n}^{c\Delta 123} = \frac{\partial W_e(\bar{\mathbf{F}}_{\text{inp}})}{\partial\bar{\mathbf{F}}_{\text{inp}}}\cdot\mathbf{N}^{c\Delta 123} = \mathbf{P}(\boldsymbol{\Delta})\cdot\mathbf{N}^{c\Delta 123}. \tag{36}$$

Note that the this expression describes both normal and tangential traction/separation in a single expression, and it is a natural mixed-mode expression. The expression of cohesive interface traction/separation law is a side product or natural consequence of APZM. In APZM, we do not need to postulate any empirical cohesive interface potential or cohesive interface constitutive relations like the conventional CZM does, i.e.

$$\mathbf{T}^{\text{coh}} = \frac{\partial W^{\text{interface}}}{\partial\boldsymbol{\Delta}} \tag{37}$$

where $W^{\text{interface}} \neq W_e$

### *3.4. The lattice structure in multiscale process zone model*

The EAM potentials for both bulk and process zone elements are given in Equations (25) and (31). They are function of bond lengths $r_{ij}$ as well as the background electron density $\rho_i$. That means: the neighboring atoms of a reference atom, i.e. its surrounding atoms in lattice ($n_b$), determine the total energy or energy density [47]. In EAM potential, the electron density item is a global effect in the N-atoms system. For metallic solids, one can benefit from nearest neighbors assumption

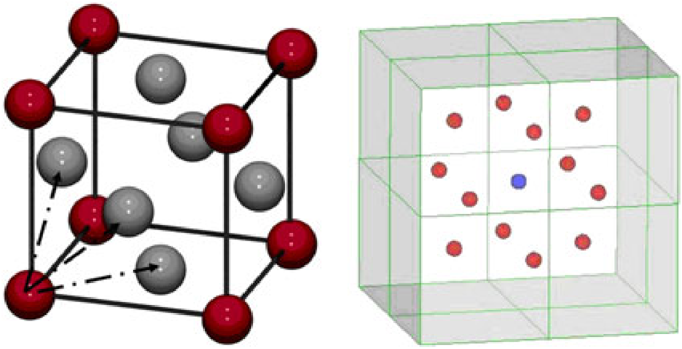

(a) (b)

Figure 5. (a) The neighboring atoms in a quadrant of a face centered cubic (FCC) unit cell; (b) the super cell for FCC lattice structure with nearest neighbors.

for computational efficiency and simplicity. Therefore, in this paper, we only consider the nearest neighbor interaction in FCC lattice shown in Figure 5.

Figure 5(a) shows the neighboring atoms in a part of FCC unit cell that contains a quadrant. To take into account of contribution of all surrounding atoms to the atomistic potential, one may add all the nearest atoms in a super cell [33,34] as shown Figure 5(b). Counting the number of surrounding atoms from Figure 5, there are 12 atoms as the nearest neighbor at

$$\begin{aligned} &\mathbf{R}_i : \left(\pm\tfrac{\sqrt{2}}{2}R_1, \pm\tfrac{\sqrt{2}}{2}R_1, 0\right) \quad && i = 1,2,3,4 \\ &\mathbf{R}_i : \left(\pm\tfrac{\sqrt{2}}{2}R_1, 0, \pm\tfrac{\sqrt{2}}{2}R_1\right) \quad && i = 5,6,7,8 \\ &\mathbf{R}_i : \left(0, \pm\tfrac{\sqrt{2}}{2}R_1, \pm\tfrac{\sqrt{2}}{2}R_1\right) \quad && i = 9,10,11,12 \\ &R_1 = |\mathbf{R}_i| && \end{aligned} \tag{38}$$

The equilibrium bond length, $R_1$, is the original atomistic bond length that is associated with equilibrium atom position without initial stress ($\mathbf{S} = 0$) and deformation ($\mathbf{F} = \mathbf{I}_3$). For FCC lattice, on the basis of Equation (38), we can find that the right-hand side of Equations (32) and (33) can be described as a scalar factor times the second-order tensor $\mathbf{R_i} \otimes \mathbf{R_i}$, where $i$ will loop over all 12 nearest surrounding atoms. When the scalar factors equal zero, we have the following relation,

$$mc\left(\sum_i \left(\frac{\alpha}{r_i}\right)^m\right)^{-0.5} \left(\frac{\alpha}{r_i}\right)^{m+2} - n\left(\frac{\alpha}{r_i}\right)^{n+2} = 0 \tag{39}$$

in bulk elements, and an additional equation,

$$(1-\beta)\left[\frac{mc}{2}\left(\sum_i \left(\frac{\alpha}{r_i}\right)^m\right)^{-0.5} \left(\frac{\alpha}{r_i}\right)^{m+2} - \frac{n}{2}\left(\frac{\alpha}{r_i}\right)^{n+2}\right] - \beta\frac{2\pi\alpha^3}{\Omega_0^b(n-2)}\left(\frac{\alpha}{r_i}\right)^{n-1} = 0 \tag{40}$$

in interphase elements, which assure that the FCC lattice is in equilibrium configuration.

We can solve the equilibrium positions, $R_1^b$ and $R_1^p$, for both bulk and process zone elements, from Equations (39) and (40), respectively. The positive root of $r_i$ will be the bound length at equilibrium position $R_1 = r_i$. Then, the volume of one atom, which occupies in FCC structure, can be calculated as

$$\Omega_0^b = \frac{\sqrt{2}}{2}\left(R_1^b\right)^3 \quad \text{and} \quad \Omega_0^p = \frac{\sqrt{2}}{2}\left(R_1^c\right)^3 \tag{41}$$

Copyright © 2012 John Wiley & Sons, Ltd.

## 4. SIMULATIONS OF FRAGMENTATION OF POLYCRYSTALLINE ALUMINUM P/M ALLOYS

In this section, we present two numerical examples by using APZM-based FEM. In the first example, we simulate fragmentation of a small cylinder that are made from aluminum powder metallurgy alloy, when it penetrates a thin plate. In the second example, the projectile is a single crystal aluminum, which behaves like a ductile material, but the plate is made of aluminum P/M alloy, and when the projectile penetrates the plate, the plate fragments.

In applications, the fragmentation process of aluminum P/M alloy has been utilized to detonate reactive materials in facilitating detonation-driven propulsion systems. It has been an outstanding challenge to devise and design such systems to obtain maximum energy release and detonation efficiency; this is because during such high-speed induced impact, fragmentation, and explosion process, it is very difficult to measure some key physical parameters of the event in experiments, for instance, how to correlate spatial dynamic fragment formation with the projectile velocity. By combining simulation-based engineering or computer-aided design with the latest development in computational nanomechanics and multiscale simulation, we may be able to precisely determine fragment size, velocity distribution, instantaneous spatial formation and its relation with impact/penetration speed, and even temperature distribution, and so on. In the case of reactive metal cylinders, the fragment's size, velocity, and its deformation state determine its ability to undergo chemical reaction upon impact loading. A successful simulation may provide fundamental understanding needed for design of explosive systems for civilian and defense applications.

### *4.1. Calibration with the experimental data*

Aluminum single crystal has FCC lattice structure, and the detonation projectile is often made of aluminum nanoparticle. In MD, the SC-EAM potential has been extensively used in modeling aluminum metals, and this is especially common for aluminum nanoparticle system. Readers may find atomistic material constants of SC-EAM potential for aluminum crystal in literature [39], listed in Table I.

In this work, the atomistic potential inside the process zone is expressed as a combination of embedded potential and depletion potential, which is explicitly given in Equation (31) with a free parameter $\beta$. In some sense, the parameter $\beta$ is a damage measurement index or depletion index of virgin material because of the presence of defects and inhomogeneities. Inhomogeneity is a physical feature of realistic polycrystalline solids. For polycrystalline aluminum P/M alloy, it is hard to quantify the global inhomogeneity state in microscale. However, in polycrystalline solids, the stiffness of grains is much higher than that of the grain boundary; drastic deformation is often observed in grain boundaries, which includes the lattice rotation, slipping, and separation of grains. Therefore, the physical properties of the grain boundary dictate the mechanical properties of polycrystalline solids. Because of extensive applications in industry, there have been many intensive researches conducted on polycrystal aluminum materials. For example, Kocks [48] gave the engineering stress–strain curve of 99.9% pure polycrystalline aluminum at different strain rates and temperature. When one uses the experimental data, different values of $\beta$ are used to calibrate the constitutive relation inside the process zone element, and the result is depicted in Figure 6. To compare with experimental data, the engineering stress (PK-I stress component $P_{22}$) along the tensile direction versus tensile deformation (u/L) are plotted. In Figure 6, the delta and square symbols show the experimental stress–strain relation at $200K$ with different strain rates reported in [48].

Table I. The material constants (SC-EAM potential) used for aluminum P/M alloy.

| $\varepsilon$ | $c$ | $\alpha$ | $m$ | $n$ |
|---|---|---|---|---|
| 3.3147e−2 eV | 16.399 | 4.05 $\AA$ | 6 | 7 |

Copyright © 2012 John Wiley & Sons, Ltd.

DOI: 10.1002/nme

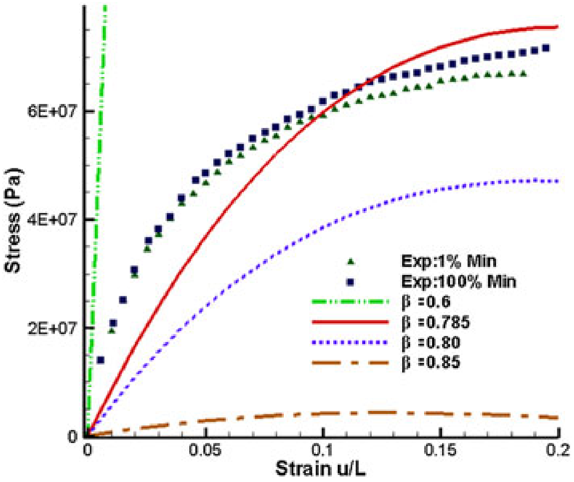

Figure 6. Calibrating $\beta$ with experimental data.

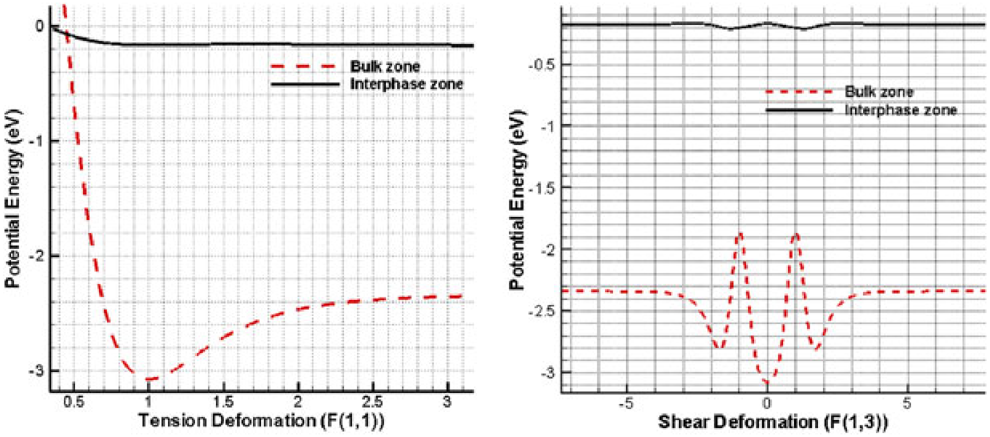

(a) (b)

Figure 7. The atomistic potential energy in bulk material and process zone: (a) under tensile deformation; (b) under shear deformation.

From Figure 6, one can find that when the portion of in-homogenous part of the process, $\beta$, increases, the process zone will become weaker sharply. We find that when we choose $\beta = 0.785$, the multiscale process zone model fits best with the experimentally measured stress–strain curve. One may find that the material in a perfect crystal bulk element ($\beta = 0.0$) is much harder than that of the process zone.

### 4.2. *Self-consistent cohesive law in polycrystalline aluminum*

Equations (33) and (35) imply that the constitutive relation inside the process zone is determined by the atomistic potential that is related to the bulk atomistic potential. By doing so, the mechanical properties inside the process zone element are consistent with the mechanical properties of the bulk element, and this is in sharp contrast with conventional cohesive zone method whose empirical cohesive laws have almost no connections to the material properties in the bulk element. Figure 7(a,b) illustrates the atomistic potential energy in both bulk elements and process zone elements under uniaxial tension and pure shear deformations, and the corresponding atomistically enriched constitutive relations are displayed in Figure 8(a,b). Here, the magnitude of stress–strain curve in the bulk element is much higher than that of the process zone; therefore, we scale down 50 times the

Copyright © 2012 John Wiley & Sons, Ltd.

DOI: 10.1002/nme

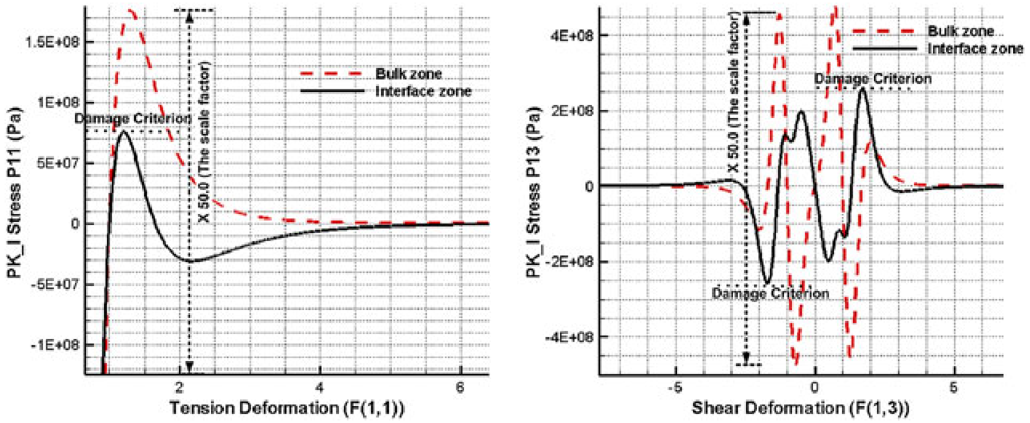

(a) (b)

Figure 8. The constitutive relations in bulk material and interphase zone: (a) under tensile deformation; (b) under shear deformation.

bulk stress value in Figure 8. From Figure 8, one may find that at early stage, the displacements of bulk element nodes controls the deformation gradient and internal stress state in process zone elements; see Equation (11). During this stage, the cohesive traction stress, Equation (16), will be balanced by the internal force of bulk elements; that is, the bulk elements are glued together by the interface element as a stable piece. Once the stress inside the process zone is over its peak value (dotted horizontal line in Figure 8) in either tension or shear deformation, the polycrystalline solid becomes unstable because the cohesive traction cannot balance the internal force of bulk elements any more while the bulk stress is still far below its peak value. At this stage, an increase of process deformation will result in a decrease of stress in process zone elements. Thereby, the adjacent bulk elements will separate automatically from each other, and local fracture of the solid occurs. Eventually, the stress in process zone will approach to zero with enormous deformation. During this fracture process, the material behaviors of bulk and process zone elements are dictated by their atomistic potentials, and fracture happens as a natural consequence of load increasing and cohesive strength decreasing without any postulated material failure criterion. This is an intrinsic advantage of proposed APZM model, which provides a natural simulation of dynamic fracture process.

Consider a simple APZM finite element mesh as shown in Figure 2, where two bulk elements sandwich one interphase element. We prescribe a mixed-model motion at the top bulk element and fix the bottom bulk element as shown in Figure 10. Here, the displacement $\Delta$ is imposed in $X$–$Z$ plane with a angle $\theta$, and $L$ is the characteristic length of process zone element. When $\theta = 0.0$, the deformation is the pure shear mode, and when $\theta = \pi/2.0$, it represents the pure tension mode. When $0 < \theta < \frac{\pi}{2}$, the deformation and the subsequent fracture are mixed mode. We plot the atomistic potential of the process zone under mixed-mode loading in Figure 9, and one can clearly see energetic transition under mixed-mode loading. Furthermore, mixed-mode energy potentials also correspond to mixed-mode stress states inside process zone; subsequently, the cohesive traction force can be calculated by the each of the stress state. Note that the PK-I stress tensor have nine components for 3D problem, and we plot the components $P_{33}$ and $P_{11}$ in Figure 10(a,b). Comparing with the conventional CZM, in which tension, shear, or mixed-mode cohesive laws are often calculated separately, this intrinsic feature of APZM indicates that the proposed APZM can solve the dynamical process under mixed fracture model naturally. This is especially crucial in realistic and massive 3D fragmentation simulations.

### 4.3. *The equilibrium bond length of FCC crystals*

The equilibrium position of a lattice depends on the lattice structure as well as the potential function. Implementing Equation (39), one can solve the equilibrium position of bulk FCC lattice with constants in Table I as

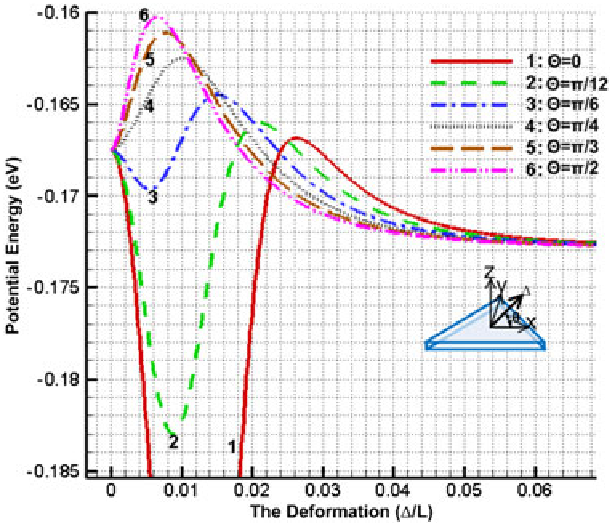

Figure 9. The atomistic energy in process zone under the mixed-model loading.

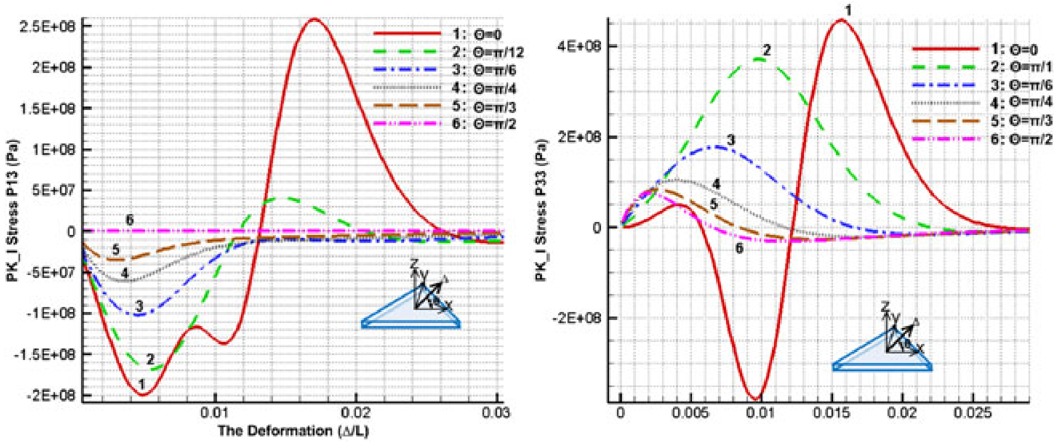

Figure 10. The PK-I stress $P_{33}$ and $P_{13}$ under mixed-mode loading.

$$R_1^b = \frac{\alpha n^{0.25} 12.0^{0.125}}{(mc)^{0.25}} \tag{42}$$

From Equation (40), one can derive a fourth-order algebraic equation:

$$\begin{aligned} a x^4 + b x + c &= 0 \\ x &= \frac{\alpha}{R_1^c} \\ a &= -0.5(1.0-\beta)n \\ b &= -\beta \frac{\sqrt{2}\pi\alpha^3}{R_1^{b\,3}(n-2)} \\ c &= 0.5(1.0-\beta)mc12^{-0.5} \end{aligned} \tag{43}$$

There are four real roots for Equation (43), which can be found by using the Ferrari method. Here, we choose the positive root

$$R_1^p = 1.30918618454348\alpha \tag{44}$$

as the equilibrium bond length.

Copyright © 2012 John Wiley & Sons, Ltd.

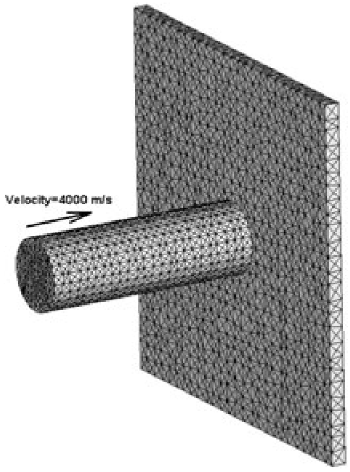

Figure 11. The configuration and finite element method mesh of projectile/target system.

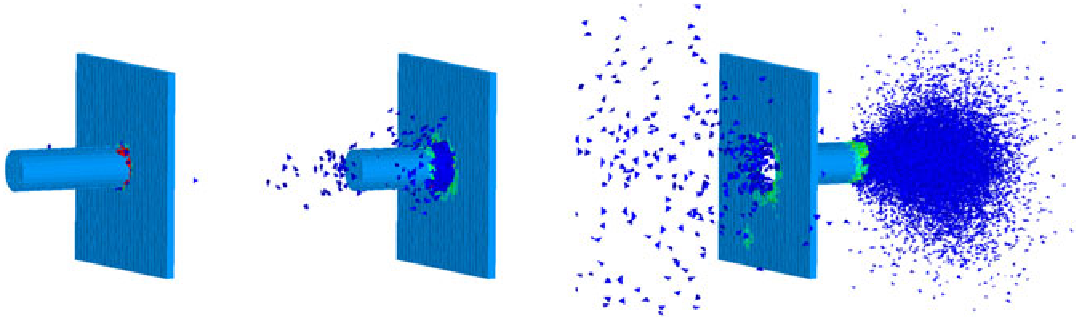

(a) $t = 0.030\mu s$. (b) $t = 0.15\mu s$. (c) $t = 0.90\mu s$.

Figure 12. The time sequence of penetration/fragmentation process with background of effective stress (perspective from the backside). (a) $t = 0.030$ $\mu$s; (b) $t = 0.15$ $\mu$s; (c) $t = 0.90$ $\mu$s.

### *4.4. Example one: penetration/fragmentation process with brittle/brittle solid impact*

With the proposed 3D APZM model, a dynamic simulation of penetration/fragmentation between polycrystalline aluminum P/M alloy cylinder and plate has been carried out. Because both cylinder and plate are modeled as polycrystalline aluminum alloy, this event is the so-called brittle/brittle fracture process. The polycrystalline aluminum cylinder (1 mm × 3 mm, diameter × length) impacts a square plate (5 mm×5 mm×0.2mm, width × height × thickness) with a very high speed 4000.0 m/s as shown in Figure 11. The shock wave induced by impact force propagates in the cylinder as well as the plate to drive the fracture process in both bodies. The material constants of the aluminum cylinder are the same as that discussed in Section 4.1, and the plate's constitutive relation has the same parameters of SC-EAM potential as the cylinder projectile except $\beta = 0.7$ in order to have a much harder target. In this simulation, grains are represented by tetrahedron with various volumes and lattice orientations; see Figure 11. Between grains, there are pentahedral process zone elements to represent grain boundary. The computational domain is discreted by $64,608$ bulk elements and $124,820$ process zone elements. In this paper, we do not discuss the impact–contact algorithm, and it is a 3D extension of the 2D contact algorithm presented in [19]. The dynamics fracture process shows Figures 12(a–c) and 13(a–f) from different perspectives. From the simulation (time) sequence plots, one may find that the propagating shock wave drives fracture in cylinder (see Figure 12(a–c)), and there are fragments formed with different velocity and rotation. Because of the high impact velocity, the fragments will penetrate the plate and spread out at the other side of plate. They move on to form a spindly fragment jet; see Figure 13(a–f). The simulated fragment formation

Copyright © 2012 John Wiley & Sons, Ltd.

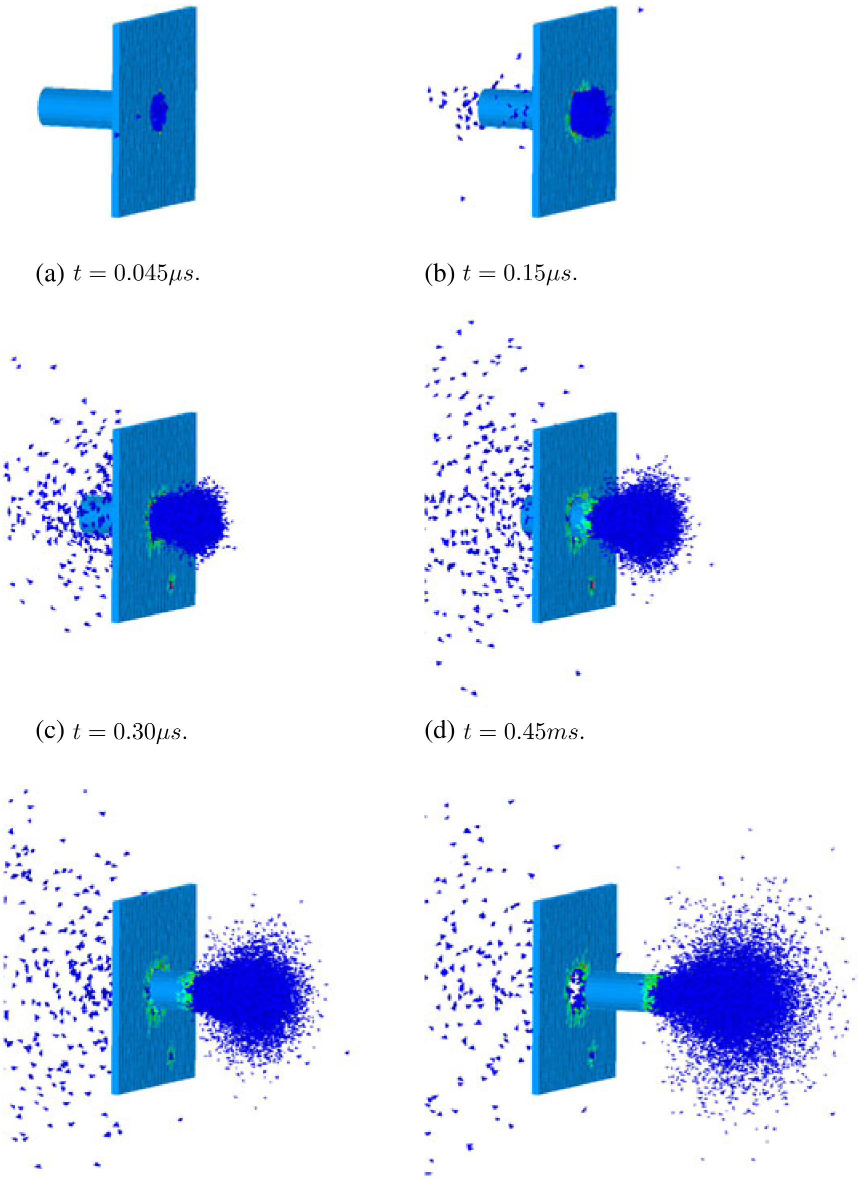

(a) $t = 0.045\mu s$.

(b) $t = 0.15\mu s$.

(c) $t = 0.30\mu s$.

(d) $t = 0.45ms$.

(e) $t = 0.60\mu s$.

(f) $t = 0.90\mu s$.

Figure 13. The time sequence of penetration/fragmentation process (perspective from the frontside). (a) $t = 0.045$ $\mu$s; (b) $t = 0.15$ $\mu$s; (c) $t = 0.30$ $\mu$s; (d); $t = 0.45$ $\mu$s; (e) $t = 0.60$ $\mu$s; (f) $t = 0.90$ $\mu$s.

demonstrates that the proposed model can capture the most complex 3D fragmentation process very well, and this particular example has been a challenging problem for other computational methods such as cohesive zone FEM, meshfree method, and extended FEM.

From Figure 10, we can find that once the stretch of a bond is over 300%, the cohesive traction force trends to zero. Therefore, to avoid the extreme deformation in interphase zone and numerical ill-condition caused by hour-glass mode, once the cohesive traction force reduces to certain value, $|\mathbf{T}^{\text{coh}}| \leqslant \delta$, we let the interphase element become invalid or being automatically deleted by implementing a cut-off function. When all the process zone elements surrounding a bulk element become invalid, that bulk element may behave like a rigid body with small elastic deformation.

Figure 8 reveals that when interphase element stretches or shears to the break point, the bulk element will always stay within elastic range with relative smaller deformation; that is, the fracture

Copyright © 2012 John Wiley & Sons, Ltd.

DOI: 10.1002/nme

process of polycrystalline solid could be considered as the separation, slip, and rotation of grains. From Figure 14(a) (the middle section of computational domain), one can find the separation and rotation of grains at damaged zone. In Figure 14(a), we can find the shock wave propagates in aluminum plate as well; the ultrasonic shock wave speed observed in this simulation is compared with that reported in experiments (see Table II), and it illustrates that the proposed method can simulate the stress wave propagation accurately.

Figure 14(b) shows the configuration of the target plate after the projectile had penetrated it. Here, we can find the zigzag damage surface of the hole. Figure 14(b) also shows a small damage zone (inside the red circle), which is induced by the impact of a fragment. This indicates that the proposed method can be used to simulate the secondary damage induced by metal jet as well. The entire spatial fragmentation formation at $t = 1.125\ \mu s$ is shown in Figure 15. One can find that more than half of the aluminum cylinder had fragmented into pieces, which forms a spindly metal jet just as

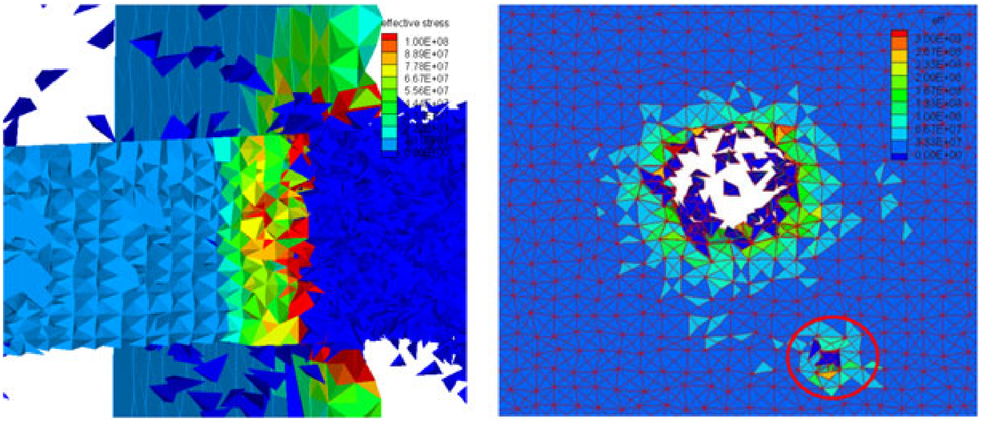

(a) (b)

Figure 14. (a) Penetration front inside the plate and (b) the damage morphology of target plate.

Table II. Wave speed in simulation and experiment.

| Wave speed in simulation | Experimental ultrasonic speed | Error |
|---|---|---|
| 6420 m/s | 6416 m/s | 0.06 % |

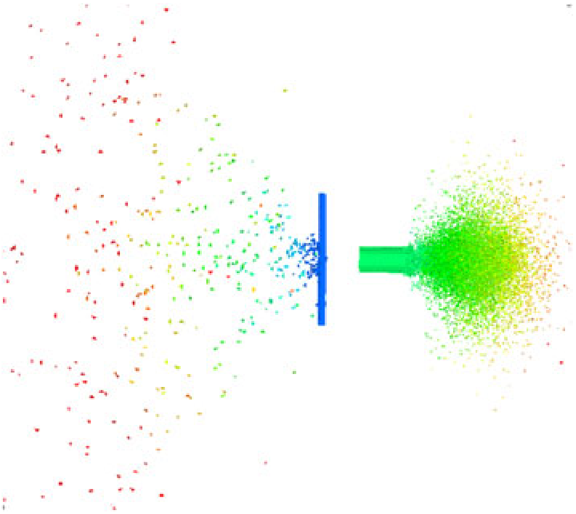

Figure 15. The spatial fragmentation formation.

Copyright © 2012 John Wiley & Sons, Ltd.

the results of macroscale high-speed brittle material impact experiment. At the opposite side, there are some fragments flying at the opposite direction; these fragments have speed from 10,000 to 70,000 m/s. The velocity distribution of fragments is plotted in Figure 16. Here, we can find most of material remain at 0.0 m/s (The target material) and about 4000.0 m/s (the original velocity of cylinder), and most of material of cylinder remains in the range velocity of 3500 to 10,000 m/s. To the best of the authors' knowledge, the impact speed of the projectile during the simulation is one of the highest that have ever been reported in the literature.

### *4.5. Example two: penetration/fragmentation process due to ductile/brittle solid impact*

In the last example, we have presented the simulation results of a fracture process during a brittle/brittle material impact/penetration with the focus on fragmentation of the bullet. In practice, there is another common type of penetration/fragmentation process that is due to ductile/brittle material impact, such as steel bullet impacts with aluminum P/M alloy plate.

In this example, we present APZM simulation results of a penetration/fragmentation process due to ductile/brittle material impact. Normally, under this scenario, the fragments are generated from brittle target—the aluminum P/M alloy plate—and the projectile will undergo dramatic plastic deformation. Therefore, the normal FEM is implemented for ductile projector, and the proposed

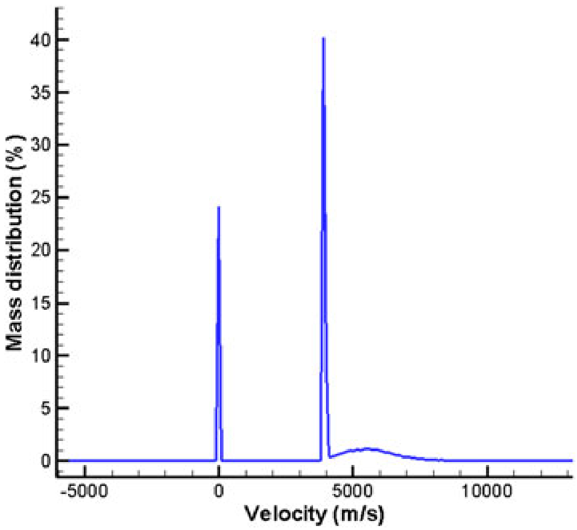

Figure 16. Velocity distribution of fragments.

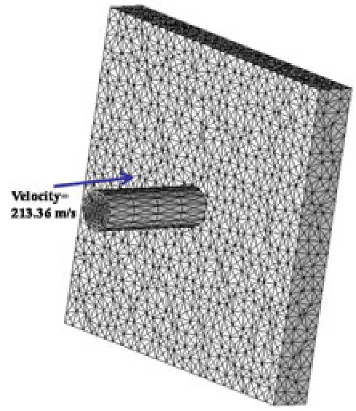

Figure 17. The configuration and finite element method mesh of projectile/target system.

Copyright © 2012 John Wiley & Sons, Ltd.

APZM model is implemented for brittle target; that is, only the target may have massive fragmentation. A cylinder shaped projectile (2.54 cm × 7.62 cm, diameter × length) impacts a target plate (19.9 cm × 19.9 cm × 2.54 cm, width × height × thickness) with speed 213.36 m/s as shown in Figure 17. The material constants of the aluminum plate are the same as that discussed in Section 4.1. Because the consideration is now focused on the fragmentation phenomenon of brittle plates, to simplify the problem, the projectile is treated as a ductile material by using a regular finite element model of single crystal aluminum material, whose material constants (SC-EAM constants) are listed in Table I.

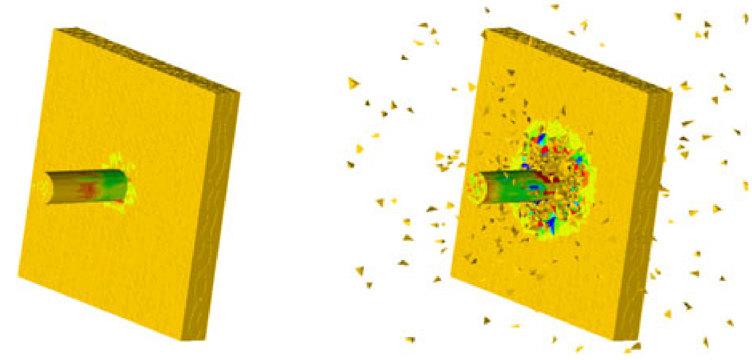

(a) $t = 3.0\mu s$.

(b) $t = 10.5\mu s$.

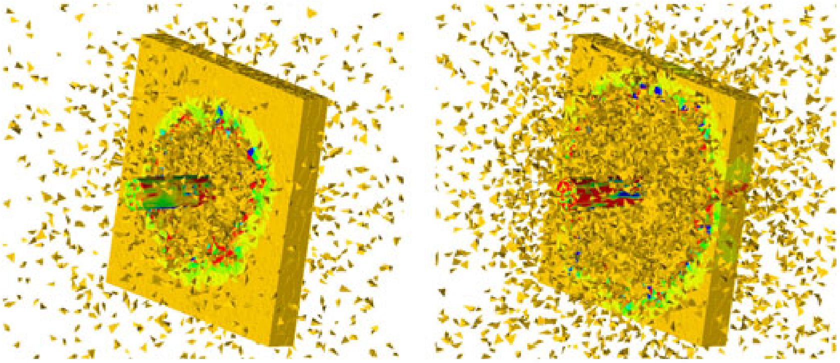

(c) $t = 16.5\mu s$.

(d) $t = 22.5ms$.

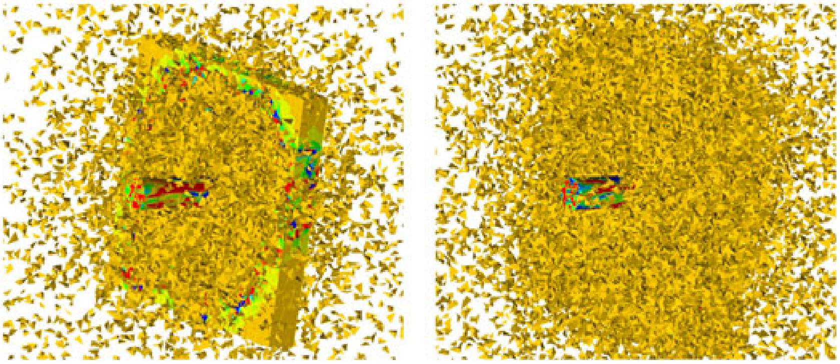

(e) $t = 25.5\mu s$.

(f) $t = 45.0\mu s$.

Figure 18. The time sequence of penetration/fragmentation process (The background color is pressure contour). (a) $t = 3.0$ $\mu$s; (b) $t = 10.5$ $\mu$s; (c) $t = 16.5$ $\mu$s; (d); $t = 22.5$ $\mu$s; (e) $t = 25.5$ $\mu$s; (f) $t = 45.0$ $\mu$s.

Copyright © 2012 John Wiley & Sons, Ltd.

The simulated dynamic fragmentation sequence is shown in Figure 18(a–f). In contrast with Example I, the target in Example II is modeled by the interphase element model; the projectile is modeled as single crystal metal with a regular FEM model without interphase elements. From Figure 8, one can find that the material stiffness of projectile is much stronger than that of the target; this results in higher wave speed and smaller deformation in the projectile. Figure 18(a) illustrates the shock wave propagates in both target and projector. For a brittle solid, the strong shock wave will drive fragmenting fracture immediately; Figure 18(b–f) show the dynamic fragmentation process along with propagation of shock wave, and eventually, the entire target is damaged. Comparing with both examples, we find that the impact velocity in Example I is extreme high, up to 4000 m/s, and that the projectile penetrates through target and punches a hole through it, whereas in Example II, the entire target breaks into pieces under a relative lower impact speed. These two different impact/fragmentation processes, shown in Figures 14 and 18, are affected by material properties of the projectile/target, impact velocity, and the size and dimension of the specimen.

A detailed projector/target penetration time sequence is shown in Figure 19(a–d), in which one may can find the damage process progresses along the shock wave propagation, and fracture occurs because of the relative rotation and translation of grains.

The results of Example I and Example II illustrate the capacity of the proposed APZM model, which can be used to simulate and predict 3D damage process of brittle polycrystalline materials. The purpose of these simulations is to explore the capability of proposed model in simulation of complex fragmentation of polycrystalline solids in virtual reality. With current experimental techniques, it is hard to capture the dynamic fracture process with high-speed impact at mesoscale sample. As shown in [30, 32], the simulation results obtained by using APZM have good agreements with MD simulation results for nanoscale simulations. On the other hand, MD will have some serious difficulties to perform 3D simulations of polycrystalline solids at mesoscale or above

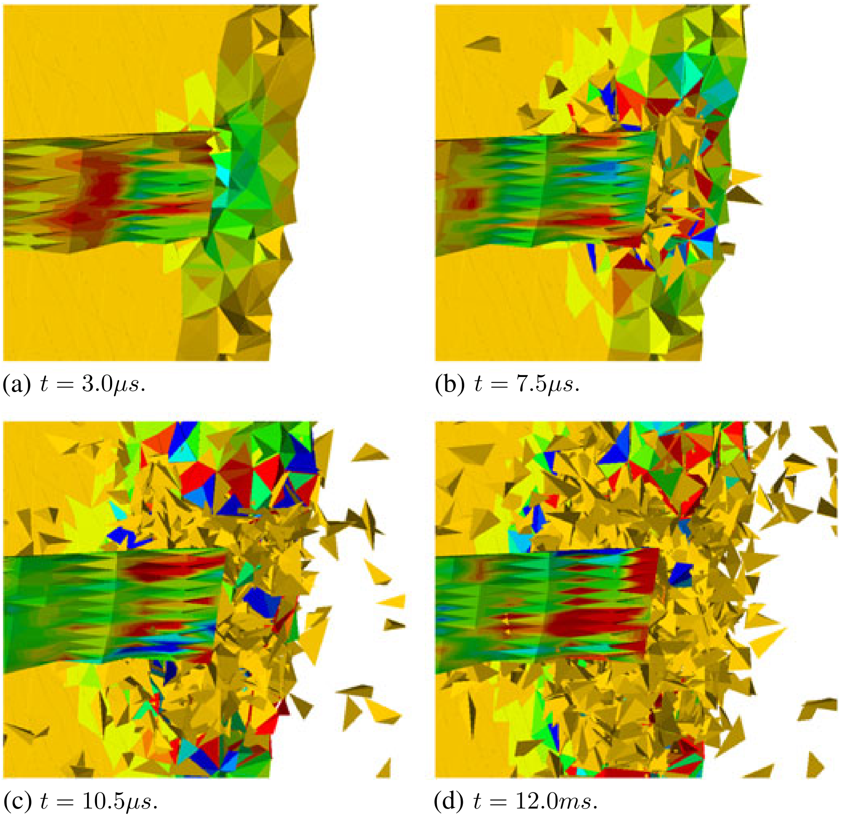
(a) $t = 3.0\mu s$.
(b) $t = 7.5\mu s$.
(c) $t = 10.5\mu s$.
(d) $t = 12.0ms$.

Figure 19. The detailed damage morphology during penetration with background of pressure. (a) $t = 3.0$ $\mu$s; (b) $t = 7.5$ $\mu$s; (c) $t = 10.5$ $\mu$s; (d); $t = 12.0$ $\mu$s.

Copyright © 2012 John Wiley & Sons, Ltd.

DOI: 10.1002/nme

because of its inherent computational cost. Whereas by using the proposed 3D APZM model, we have successfully simulated fracture process in reasonably large-scale polycrystalline solids, and the basic formulations and material constants within are all derived on the basis of the atomistic feature of the solid. The preliminary results have shown that APZM simulation can predict a reasonable accurate and stable fragmentation formation and damage/fracture morphology.

## 5. CONCLUSIONS

In this paper, we present the theoretical analysis and numerical implementation of a 3D atomistic-based multiscale interphase FEM with an EAM potential. This model is capable to simulate the complex fracture process of polycrystalline solids as penetration/fragmentation at both mesoscale and macroscale.

Comparing with the conventional CZM, the present method has some advantages: first, an atomistic enriched potential is constructed to represent the constitutive relation of polycrystalline solids in grain boundary. This potential is derived from the realistic EAM potential in grains employing the basic principle of colloidal physics, and it is self-consistent with the bulk grain potential. Second, with the atomistic potentials in bulk and interphase zone, the self-consistent cohesive law can be derived for all deformation components from underneath atomistic structure, contrasting with conventional cohesive zone method, which constructs empirical cohesive law at tensional and tangential direction only. This feature indicates that the proposed model can handle the complex fracture process under mixed loadings. Third, instead of using engineering constitutive relation at macroscale, the constitutive relations of grain and grain boundary are derived from the atomistic potential by using the Cauchy–Born rule at mesoscale. Finally, the metallic material failure is the consequence of the interatomic interaction at microscale; the EAM potential used in proposed model can describe it accurately with computational efficiency.

It has been shown that the fragmentation simulation presented here can capture complex 3D fracture process very well because the proposed method is able to take into account some essential material information such as atomistic potential, lattice structure, and mixed-mode fracture, even though there are still some more work to do. First, the shapes of grains in brittle polycrystalline solids [4] are much more complex than just tetrahedron, which is used to simplify the shape of grains in this work. As the Voronoi tessellation is often used to represent 2D polycrystals [3, 5], a 3D random Voronoi tessellation should be used to construct 3D polycrystalline finite element mesh. Second, the nonlinear deformation field around a crack tip is approximated by piece-wise uniform deformation in this work. To improve accuracy and fidelity, the higher order bulk and interphase elements may have to be adopted instead of the uniform deformation tetrahedral and pentahedral elements. More importantly, to ensure simulation results convergence, one has to introduce physical meaningful length scale that is related to the problem being simulated. We shall address this and other related issues in a separated paper.

## ACKNOWLEDGEMENT

This work is supported by a grant from Office of Naval Research (ONR) to NextGen Aerospace Co., which subcontracted to the University of California at Berkeley.

## REFERENCES

1. Belytschko T, Parimi C, Moes N, Sukumar N, Usui S. Structured extended finite element methods for solids defined by implicit surfaces. *International Journal for Numercal Methods in Engineering* 2003; **56**:609C635.
2. Clayton JD. Modeling dynamic plastic and spall fracture in high-density polycrystalline alloys. *Internal Journal of Solids and Structure* 2005; **42**:4613–4640.
3. Qian J, Li S. Application of multiscale cohesive zone model ASME. *Journal of Engineering Materials Technology* 2011; **133**(1):011010-1-10.
4. Espinosa HD, Zavattieri PD. A grain level model for the study of failure initation and evolution in polycrystalline brittle materials. Part I: theory and numerical implementation. *Mechanics of Materials* 2003a; **35**:333–364.
5. Espinosa HD, Zavattieri PD. A grain level model for the study of failure initation and evolution in polycrystalline brittle materials. Part II: numberical examples. *Mechanics of Materials* 2003b; **35**:365–394.

Copyright © 2012 John Wiley & Sons, Ltd.

6. Addessio F, Johnson J. A constitutive model for the dynamic response of brittle materials. *LA-UR-89-2651*, Alamos National Laboratory, 1999.
7. Curran D, Seaman L, Cooper T, Shockey D. Micromechanical model for comminution and granulr flow of brittle material under highstrain reate application to penertation of ceramic targets. *International Journal of Impact Engineering* 1990; **53**:53–83.
8. Lawn B. *Fracture of Brittle Solid*. Cambridge University press: Cambridge, UK, 1993.
9. Schlick T. *Molecular Modeling and Simulation: An Interdisciplinary Guide*. Springer-Verlag New York, Inc.: Secaucus, USA, 2002.
10. Abraham FF, Broughton JQ, Bernstein N, Kaxiras E. Spanning the continuum to quantum length scales in a dynamic simulation of brittle fracture. *Europhysics Letters* 1998; **44**(6):783–787.
11. Xiao SP, Belytschko T. A bridging domain method for coupling continua with molecular dynamics. *Computer Methods in Applied Mechanics and Engineering* 2004; **193**:1645–1669.
12. Park HS, Karpov EG, Liu WK, Klein PA. The bridging scale for three-dimensional atomistic/continuum coupling. *Philosophical Magazine* 2005; **85**:79–113.
13. Chen Y, Lee JD. Atomistic formulation of a multiscale field theory for nano/micro solids. *Philosophical Magazine* 2007; **85**:4095–4126.
14. Lee JD, Wang X, Chen Y. Multiscale material modeling and its application to a dynamic crack propagation problem. *Theoretical and Applied Fracture Mechanics* 2009; **51**:33–40.
15. Chen J, Wang X, Wang H, Lee JD. Multiscale modeling of dynamic crack propagation. *Engineering Fracture Mechanics* 2010; **77**:736–743.
16. Grah M, Alzebdeh K, Sheng P, Vaudin M, Bowman K, Ostoja-Starzewki M. Brittle intergranular failure in 2D microstructures: experiments and computer simulations. *Acta Mater* 1996; **44**(10):4003–4018.
17. Zikry M, Kao M. Inelastic microstructural failure mechanisms in crystalline materials with high angle grain boundaries. *Journal of the Mechanics and Physics of Solids* 1996; **44**(11):1765–1798.
18. Mose N, Dolbow J, Belytschko T. A finite element method for crack growth without remeshing. *International Journal for Numerical Methods in Engineering* 1999; **46**:131C150.
19. Ren B, Li S. Meshfree simulations of plugging failures in high-speed impacts. *Computers and Structures* 2010; **88**:909–923.
20. Ren B, Li S. Meshfree simulations of spall fracture. *Computer Methods in Applied Mechanics and Engineering* 2011; **200**:797–811.
21. Xu XP, Needleman A. Numerical simulations of fast crack growth in brittle solids. *Journal of the Mechanics and Physics of Solids* 1994; **42**:1397–1434.
22. Dugdale DS. Yielding of steel sheets containing slits. *Journal of the Mechanics and Physics of Solids* 1960; **8**:100C104.
23. Barrenblatt GI. The mathematical theory of equilibrium of cracks in brittle fracture. *Advances in Applied Mechanics* 1962; **7**:55–129.
24. Van den Bosch MJ, Schreurs PJG, Geers MGD. An improved description of the exponential Xu and Needleman cohesive zone law for mixed-mode decohesion. *Engineering Fracture Mechanics* 2006; **73**(9):1220–1234.
25. Hayes R, Ortiz M, Carter E. Universal binding-energy relation for crystals that accounts for surface relaxation. *Physical Review B* 2004; **69**:172104.
26. Braides A, Adrian JL, Michael O. Effective cohesive behavior of layers of interatomic planes. *Archive for Rational Mechanics and Analysis* 2006; **180**:151–182.
27. Liu X, Li S, Sheng N. A cohesive finite element for quasi-continua. *Computational Mechanics* 2008; **42**:543–553.
28. Chevrier P, Klepaczko JR. Spall fracture: mechanical and microstructural aspects. *Engineering Fracture Mechanics* 1999; **63**:273–294.
29. Ortiz M, Pandolfi A. Finite-deformation irreversible cohesive elements for three-dimensional crack-propagation analysis. *International Journal for Numerical Methods in Engineering* 1999; **44**:1267–1282.
30. Zeng X, Li S. A multiscale cohesive zone model and simulations of fractures. *Computer Methods in Applied Mechanics and Engineering* 2010; **199**:547–556.
31. Li S, Zeng X, Ren B, Qian J, Zhang J, Jha AJ. An atomistic-based interphase zone model for crystalline solids. *Computer Methods in Applied Mechanics and Engineering* 2012; **229-232**:87–109.
32. He M, Li S. An embedded atom hyperelastic constitutive model and multiscale cohesive finite element method. *Computational Mechanics* 2012; **49**:337–355.
33. Daw MS, Foiles SM, Baskes MI. The embedded-atom method: a review of theory and applications. *Materials Science Reports* 1993; **9**(7–8):251–310.
34. Daw MS, Baskes MI. Semiempirical, quantum mechanical calculation of hydrogen embrittlement in metals. *Physical Review Letters* 1983; **50**(17):1285–1288.
35. Daw MS, Baskes MI. Embedded-atom method: derivation and application to impurities, surfaces, and other defects in metals. *Physical Review B* 1984; **29**(12):6443–6453.
36. Yuan XJ, Chen NX, Shen J, Hu W. Embedded-atom-method interatomic potentials from lattice inversion. *Journal of Physics: Condensed Matter* 2010; **22**(37):375–503.
37. Oh DJ, Johnson RA. Simple embedded atom method model for FCC and HCP metals. *Journal of Materials Research* 1992; **3**(3):471–478.

Copyright © 2012 John Wiley & Sons, Ltd.

38. Johnson RA, Oh DJ. Analytic embedded atom method model for BCC metals. *Journal of Materials Research* 1989; **4**:1195–1201.
39. Pelaez S, Garcia-Mochales P, Serena PA. A comparison between EAM interatomic potentials for Al and Ni: from bulk systems to nanowires. *Physica Status Solidi (a)* 2006; **203**(6):1248–1253.
40. Mei J, Davenport JW, Fernando GW. Analytic embedded-atom potentials for fcc metals: application to liquid and solid copper. *Physical Review B* 1991; **43**(6):4653–4658.
41. Borst RD, Gutirrez MA, Wells GN, Remmers JJC, Askes H. Cohesive-zone models, higher-order continuum theories and reliability methods for computational failure analysis. *Journal for Numerical Methods in Engineering* 2004; **60**:289–315.
42. Hill R. On constitutive macro-variables for heterogeneous solids at finite strain. *Proceedings of Royal Society of London* 1972; **A 326**:131–147.
43. Belytschko T, Liu WK, Moran B. *Nonlinear Finite Elements for Continua and Structures*. Wiley: Chichester, 2000.
44. Kaxiras E. *Atomic and Electronic Structure of Solids*. Cambridge University press: Cambridge, UK, 2003.
45. Liu XY, Ercolessi F, Adams JB. Aluminium interatomic potential from density functional theory calculations with improved stacking fault energy. *Modelling and Simulation in Materials Science and Engineering* 2004; **12**:665670.
46. Israelachvili J. *Intermolecular and Surface Forces*, Second Edition. Academic Press: New York, 1992.
47. Baskes MI. Modified embedded-atom potentials for cubic materials and impurities. *Physical Review B* 1992; **46**:2727–2742.
48. Kocks UF. Laws for work-hardening and low-temperature creep. *Journal of Engineering Materials and Technology* 1976; **98**(1):76–86.

Copyright © 2012 John Wiley & Sons, Ltd.

DOI: 10.1002/nme